Seeded Growth of Metal Nitrides on Noble Metal Nanoparticles to Form Complex Nanoscale Heterostructures

Robert W. Lord, Cameron F. Holder, Julie L. Fenton, and Raymond E. Schaak*

Department of Chemistry and Materials Research Institute, The Pennsylvania State University, University Park, PA 16802, United States

ABSTRACT: Colloidal heterostructured nanoparticles that integrate multiple materials through direct solid-solid interfaces are desirable across a wide range of applications. However, chemical, structural, interfacial, and synthetic considerations have limited the scope of materials that can be incorporated into such hybrid constructs. Metal nitrides are appealing components of heterostructured nanoparticles because of their unique and diverse electronic, photonic, and catalytic properties, but they can be challenging to synthesize. Here, we demonstrate that the model metal nitride systems Cu_3N and Cu_3PdN can be grown in solution on various noble metal seed particles to form a library of heterostructured metal–metal nitride nanoparticles. The types of nanoscale heterostructures that form depend on both the morphology of the noble metal seed particle and the material being deposited. The pathway by which Cu_3PdN grows on Pt nanocube seeds involves initial nonselective deposition of Cu, followed by localized deposition of Pd at the corners along with concomitant incorporation of nitrogen and crystallization of Cu_3PdN. Preferential Pd deposition at seed particle corners therefore drives regioselectivity during the growth of Cu_3PdN, leading to the formation of Pt–Cu_3PdN heterostructured nanoparticles. For seed particles that are not highly faceted, as well as Cu_3N, localized deposition is not observed, and different types of core-shell and alloy nanoparticles form. Cu_3PdN also deposits selectively on the exposed corners of the cube-shaped Pt domains of Pt–Fe_3O_4 hybrid nanoparticles, forming complex Fe_3O_4–Pt–Cu_3PdN heterotrimers. These observations provide useful insights for incorporating metal nitrides into nanoscale heterostructures using seeded growth processes.

Introduction

Colloidal heterostructured nanoparticles that integrate multiple materials through solid-solid interfaces are foundational components of applications as diverse as catalysis, plasmonics, solar energy conversion, magnetism, theranostics, and biomedical imaging.[1-12] While each constituent material in a multicomponent nanoparticle has a function, the heterointerfaces permit electronic coupling and enable the emergence of synergistic properties that the individual particles cannot achieve on their own. For example, heterostructured Fe_3O_4-CdS@Au nanoparticles exhibit enhanced photothermic-catalytic activity for water reduction, and core-shell fct-PdFe@Pd nanoparticles supported on graphene function as highly efficient catalysts for the oxygen reduction reaction (ORR).[10, 13] The development of methods to synthesize colloidal heterostructured nanoparticles must consider the chemistry needed to form the desired materials, the compatibility of chemical reagents and reaction conditions with other materials that are present, and the ability to form a stable interface. Seeded growth methods, where one material grows off another in solution, have been used to synthesize various types of hybrid, asymmetric, core-shell, and nanocage constructs.[4, 5, 14, 15] Nanoparticle coupling reactions, phase segregation reactions, and partial cation exchange reactions provide additional pathways to colloidal heterostructured nanoparticles.[4, 16-18] However, despite these and other approaches, the diversity of materials that can be incorporated into colloidal heterostructured nanoparticles remains limited predominantly to metals, metal alloys, metal oxides, metal chalcogenides, and metal halide perovskites.[5, 7, 12, 13, 19-21] Other important classes of materials remain conspicuously absent.

Among the classes of materials that have not yet been incorporated into colloidal heterostructured nanoparticles are metal nitrides, which are important for a variety of applications that include catalysis, electro-optics, and energy conversion and storage.[22-25] Metal nitrides are notoriously difficult to synthesize as colloidal nanoparticles because the most readily available nitrogen sources, including ammonia, amides , and N_2, are not generally reactive at the maximum temperatures that can be achieved in the solvents that are typically used in nanoparticle synthesis.[23, 26-28] Of the few metal nitride nanoparticles that have been made colloidally, Cu_3N and Cu_3PdN are ideal material components to incorporate into heterostructured nanoparticles. Both of these materials are readily accessible at moderate temperatures in solution.[28] It has been reported that the use of nitrate

salts help to facilitate the formation of the metal nitrides when synthesized in the presence of alkylamines,[29] and also that ammonia may be evolved through reduction of an alkyl imine formed *in situ*.[30] Additionally, key reagents used to synthesize these materials, including oleylamine and 1-octadecene, are common to other nanoparticle systems, which ensures chemical compatibility with other nanoparticles already present in solution and allows seeded growth to occur. Cu_3N and Cu_3PdN, which have been identified as useful non-platinum catalysts for the ORR in alkaline media, are also valuable targets to incorporate into heterostructured nanoparticles, which contain interfaces that can modulate catalytic properties.[22, 28]

Here, we show that the colloidal metal nitrides Cu_3N and Cu_3PdN can be grown on Pt and Au nanoparticle seeds to form a diverse range of nanoscale heterostructures. Cu_3PdN grows on faceted Pt seeds through *in situ* deposition of a Cu-rich intermediate followed by incorporation of Pd and N at the corners. In contrast, the growth of Cu_3N on Pt appears more sluggish and indiscriminate. These observations reveal a synthetic pathway for achieving the regioselective deposition of metal nitrides onto noble metal nanoparticle seeds. These insights can be applied to the rational design of more complex multicomponent heterostructures such as Fe_3O_4–Pt–Cu_3PdN. In addition to serving as instructive metal nitride–noble metal model systems that provide important insights into the seeded growth pathway, these heterostructures integrate various catalytic and plasmonic nanomaterials and therefore may serve as future platforms for constructing multi-functional hybrid constructs.

Experimental Section

Chemicals and Materials. Copper(II) nitrate trihydrate [$Cu(NO_3)_2{\cdot}3H_2O$, 99+%], gold(III) chloride hydrate [$HAuCl_4{\cdot}xH_2O$, 99.995%], platinum(II) acetylacetonate [$Pt(acac)_2$, 97%], iron(0) pentacarbonyl [$Fe(CO)_5$, 99.99+%], iron(III) acetylacetonate [$Fe(acac)_3$, 99.7%], borane *tert*-butylamine complex (BTB, 97%), benzyl ether (98%), oleic acid (OLAC, 90%, technical grade), oleylamine (OLAM, 70%, technical grade), and 1-octadecene (ODE, 90%, technical grade) were purchased from Sigma-Aldrich. Palladium(II) acetylacetonate [$Pd(acac)_2$, 99%] was purchased from Strem Chemicals. Solvents (hexanes, toluene, ethanol, and acetone) were of analytical grade. All chemicals were used as received without further purification.

General safety considerations. It should be noted that as with all metal nanoparticle reactions synthesized at elevated temperatures in high boiling point solvents, it is important to ensure safety through proper training and chemical handling, implementation of procedures and techniques, and careful monitoring of in-progress reactions. These reactions involve corrosive chemicals, heated flammable liquids that must be kept under air-free conditions, various redox reactions, and gas evolution that can cause bumping, including water vapor and CO from $Fe(CO)_5$.

Synthesis of 8-nm Cube-Shaped Pt Nanoparticles. Using a modification of a reported procedure, 100 mg (0.25 mmol) of $Pt(acac)_2$, 10 mL of ODE, 1 mL OLAM, and 1 mL OLAC were added to a three-necked, 50-mL round-bottom flask equipped with a magnetic stir bar, reflux condenser, thermometer, and rubber septum.[31] The mixture was placed under vacuum and degassed at 120 °C for 30 minutes. The reaction mixture was then placed under an Ar blanket. In an Ar-filled glovebox, a solution of 15 µL of $Fe(CO)_5$ in 1 mL of benzyl ether was added to a 20-mL septum-capped vial. The Fe precursor solution was then injected by syringe into the main reaction mixture. The reaction vessel was then heated to 190 °C (at a rate of 5-10 °C/min). The reaction mixture was aged at 190 °C for 1 hour, and then the reaction vessel was removed from the heating mantle and allowed to cool to room temperature. The formed particles were precipitated by ethanol and collected by centrifugation. The particles were redispersed in hexanes, precipitated by adding ethanol, and centrifuged again. The collected particles were dispersed in hexanes and stored for further use.

Synthesis of 6-nm Multifaceted Pt Nanoparticles. The procedure to synthesize the 5-nm multifaceted Pt particles was the same as that described above to synthesize the 8-nm cube-shaped Pt nanoparticles, except that after degassing at 120 ºC for 30 minutes and placing the reaction mixture under an Ar blanket, the reaction mixture was additionally heated to 180 ºC before injecting $Fe(CO)_5$.

Synthesis of 7-nm Au Nanoparticles. Using a modification of a reported procedure, 100 mg (0.29 mmol) of $HAuCl_4{\cdot}xH_2O$, 10 mL of OLAM, and 10 mL of toluene were loaded into a 40-mL vial with a magnetic stir bar.[32] The mixture was stirred, open to air, for approx. 5 minutes. A solution of 50 mg (0.57 mmol) of TBAB in 2 mL of a 1:1 (v/v) mixture of OLAM and toluene was added to the gold solution. The reaction mixture was aged at room temperature for 1 hour. The formed particles were precipitated by ethanol and collected by centrifugation. The particles were dispersed in hexanes and precipitated by adding ethanol and centrifuged again. The collected particles were dispersed in hexanes and stored for further use.

Synthesis of M–Cu_3PdN (M = Pt, Au) Heterostructured Nanoparticles. Using a modification of a reported procedure, 60 mg (0.25 mmol) of $Cu(NO_3)_2{\cdot}3H_2O$, 25 mg of $Pd(acac)_2$, 7.5 mL of ODE, 2.5 mL of OLAM, and 10 mg of metal nanoparticles were added to a three-necked, 50-mL round-bottom flask equipped with a reflux condenser, thermometer adapter, thermometer, rubber septum, and magnetic stir bar.[28] The reaction mixture was placed under vacuum and degassed at 120 °C for 1 hour. The solution was then placed under an Ar blanket then heated to 190 °C (at a rate of 5-10 °C/min). The solution was aged at 190 °C for 30 minutes, and then the reaction vessel was removed from the heating mantle and allowed to cool to room temperature. The formed particles were precipitated with ethanol and then collected by centrifugation. The particles were redispersed in

hexanes and precipitated by adding ethanol and centrifuged again. The collected particles were dispersed in hexanes and stored for further characterization.

Synthesis of Pt–Fe_3O_4 Hybrid Nanoparticles. Using a modification of a reported procedure, 50 mg (0.14 mmol) of $Fe(acac)_3$, 4 mL OLAC, 6 mL OLAM, and 5 mg of Pt nanoparticle seeds were added to a three-necked, 50-mL round-bottom flask equipped with a reflux condenser, thermometer adapter, thermocouple, rubber septum, and magnetic stir bar.[33] The reaction mixture was placed under vacuum and degassed at 120 °C for 30 minutes. The solution was then placed under an Ar blanket then heated to 310 °C and reacted at this temperature for 30 minutes. The reaction vessel was removed from the heating mantle and allowed to cool to 60 °C. The formed particles were precipitated with ethanol and then collected by centrifugation. The particles were redispersed in hexanes and precipitated by adding ethanol and centrifuged again. The collected particles were dispersed in hexanes and stored for further characterization.

Synthesis of Cu_3PdN–Pt–Fe_3O_4 Heterotrimer Nanoparticles. The reaction conditions were the same as for the synthesis of Pt–Cu_3PdN heterostructured nanoparticles except for using 12 mg of the Pt–Fe_3O_4 hybrid nanoparticles as seeds and a reaction time and temperature of 15 minutes at 170 °C.

Materials Characterization. Transmission electron microscopy (TEM) images were collected on a JOEL 1200 EX II microscope operating at 80 kV. High-resolution transmission electron microscopy (HRTEM) images, unless otherwise stated, were collected on a FEI Titan G2 S/TEM equipped with spherical aberration correctors on the image and probe-forming lenses at an accelerating voltage of 200kV. Unless otherwise indicated, high angle annular dark field scanning transmission electron microscopy (HAADF-STEM), STEM energy dispersive X-ray spectroscopy (STEM-EDS) maps, and selected area electron diffraction (SAED) patterns were collected on a FEI Talos F200x S/TEM at an accelerating voltage of 200 kV. ImageJ software was used to analyze the SAED and HRTEM images. Bruker ESPIRIT 2 software was used to interpret the STEM-EDS element map data. Powder X-ray diffraction (XRD) data were collected on a Bruker D-8 Advance X-ray diffractometer using Cu Kα radiation. X-ray photoelectron spectra (XPS) were collected on a PHI VersaProbe II spectrometer, equipped with a scanning monochromatic Al Kα X-ray source ($h\nu$ = 1486.6 eV) and a concentric hemispherical analyzer. Charge neutralization was performed using both low energy electrons (<5 eV) and argon ions. The binding energy axis was calibrated using sputter cleaned Cu foil (Cu $2p_{3/2}$ = 932.7 eV, Cu $3p_{3/2}$ = 75.1 eV). Survey and high-resolution scans were acquired at pass energies of 117.4 eV and 29.4 eV, respectively. Peaks were charge referenced to C 1s at 284.8 eV. Measurements were made at a takeoff angle of 45° with respect to the sample surface plane. This resulted in a typical sampling depth of 306 nm (95% of the signal originated from this depth or shallower). Quantification was done using instrumental relative sensitivity factors (RSFs) that account for the X-ray cross section and inelastic mean free path of the electrons.

Results and Discussion

Deposition of Cu_3N and Cu_3PdN on Pt and Au Nanoparticles. Cu_3N nanoparticles were synthesized by reacting $Cu(NO_3)_2$ in 1-octadecene and oleylamine at 210 °C and Cu_3PdN nanoparticles were synthesized by reacting $Cu(NO_3)_2$ and $Pd(acac)_2$ in 1-octadecene and oleylamine at 190 °C as described in detail in the Experimental Section and as confirmed by the TEM and XRD data in Figures 1 and S1. We then used these same reagents and reaction conditions to attempt to grow Cu_3N and Cu_3PdN in the presence of various types of Pt and Au nanoparticle seeds to produce heterostructure nanoparticles having metal nitride–noble metal interfaces. Figure 1 shows TEM images of the three types of Pt and Au nanoparticle seeds: 8-nm cube-shaped Pt particles, 6-nm multi-faceted Pt particles, and 7-nm spherical Au particles. Figure 1 also shows TEM images of the products formed after the attempted growth of Cu_3N and Cu_3PdN using the established conditions mentioned above. The observed morphologies reveal interesting similarities and differences among the various systems. For the spherical Au seeds, Cu_3PdN uniformly covers the Au particle to form core-shell particles. For the multi-faceted Pt seeds, a range of heterostructures is observed, including core-shell particles for more spherical Pt seeds and particles having Cu_3PdN localized on the more faceted regions. For the cube-shaped Pt particles, the Cu_3PdN appears to be localized exclusively on the corners of the Pt nanocubes. The growth behavior of Cu_3N on the various Pt and Au seeds is quite different than for Cu_3PdN. For all types of Pt seeds, there appears to be little preference to where the Cu_3N grows under established conditions, forming predominantly core-shell structures. Cu_3N was not observed to grow on Au seeds under established conditions. In contrast, XRD data indicate the formation of a AuCu alloy instead of discreet Au and Cu_3N domains (Figures 1 and S2).

Based on the data in Figure 1, where attempts to seed the growth of Cu_3N and Cu_3PdN on various Pt and Au nanoparticles used the reaction conditions that were already established for the synthesis of Cu_3N and Cu_3PdN nanoparticles, two sets of observations are especially notable. First, Cu_3N does not grow on Au seeds under these reaction conditions, favoring alloy formation instead of seeded growth, while Cu_3N growth on Pt occurs indiscriminately to form core-shell particles rather than regioselectively on certain facets. Second, while Cu_3PdN does indeed grow on both the Pt and Au seeds, the morphology of the seeds, and in particular the faceting, influences the regions of the particle surface where nitride growth occurs. These results point to differences in the growth pathways for the various systems, as well as the possibility of achieving regioselectivity during seeded growth, and therefore motivate a deeper study of the pathways by which the metal nitrides grow on noble metal seeds.

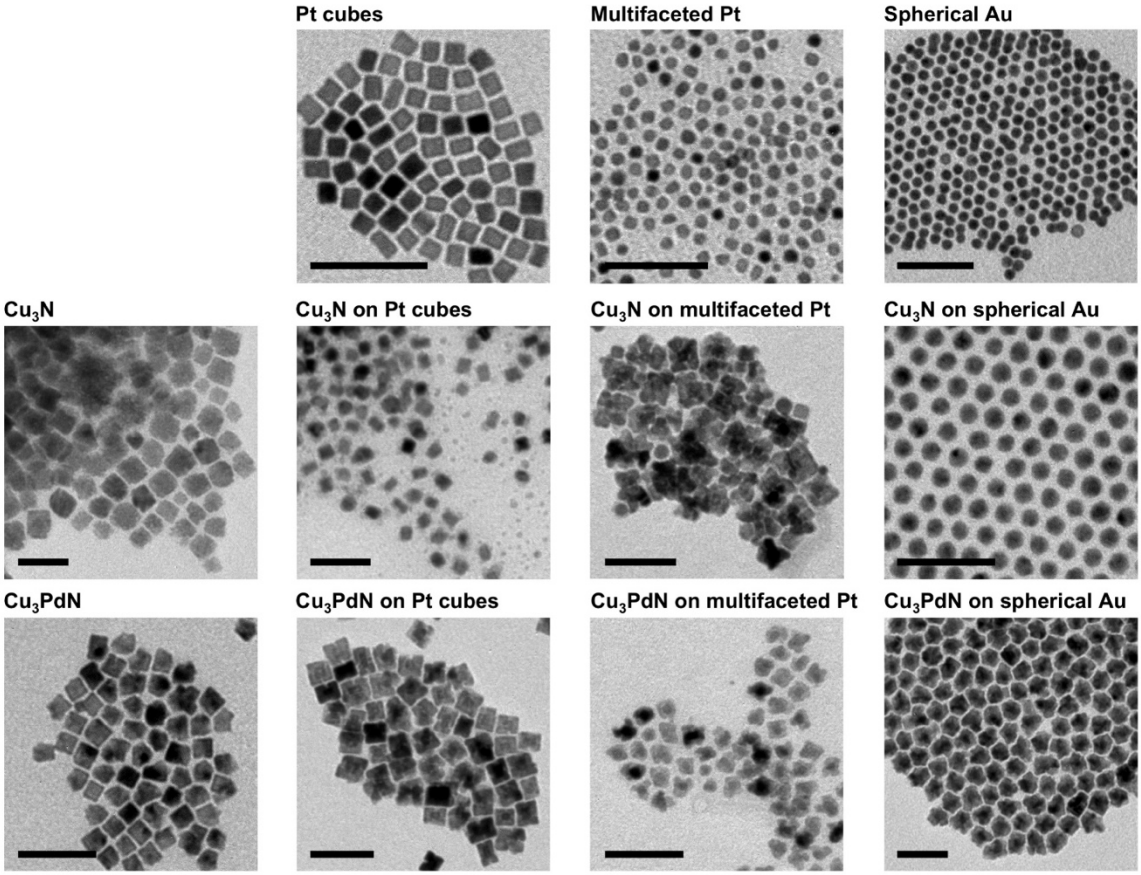

Figure 1. TEM image grid showing (top) the various Pt and Au nanoparticle seeds, (left) Cu_3N and Cu_3PdN nanoparticles synthesized directly without noble metal seeds present, and (other panels) heterostructured nanoparticles formed by growing Cu_3N and Cu_3PdN on the various Pt and Au seeds. All scale bars correspond to 50 nm.

Growth Pathway of Cu_3PdN on Pt Nanocubes. The growth of Cu_3PdN on Pt nanocubes provides an instructive model system for elucidating the pathway by which metal nitrides grow regioselectively on noble metal seeds. To monitor the growth process, samples from three individual reactions, run in parallel under identical conditions, were obtained by quenching 1) when the reaction reached 170 ºC (the point at which the solution was observed to darken), 2) when the reaction reached 190 ºC (the temperature at which Cu_3PdN forms), and 3) after the reaction was held for 30 min at 190 ºC (complete reaction). Figure S3 shows TEM images for each sample. At 170 ºC, the Pt seeds appear unchanged by TEM, suggesting that seeded growth has not yet occurred. However, at 190 ºC, both initially and after 30 min, there is evidence of significant seeded growth, with cube-shaped particles growing off the corners of the Pt nanocubes. This indicates that growth occurs rapidly in the range of 170 ºC to 190 ºC.

To better probe the early stages of growth between 170 ºC and 190 ºC, we generated five additional samples by holding the reactions at 170 ºC and quenching after 5, 10, 15, 60, and 120 minutes. Figure 2 shows HRTEM, HAADF-STEM, and STEM EDS data for the 5, 10, and 15-minute samples; HAADF-STEM and STEM EDS data for the 60 and 120-minute samples are shown in Figure S4 of the Supporting Information. After 5 minutes at 170 ºC (Figure 2a-f), no visible surface deposits are observable microscopically. However, STEM-EDS element maps indicate that the surface is covered with Cu, which is consistent with the darkening of the solution. No Pd is present in the particles at this stage. After 10 minutes at 170 ºC (Figure 2g-l), the HRTEM and HAADF-STEM images reveal a lighter-contrast shell surrounding the darker-contrast Pt seeds, and the shell correlates with the Cu signal in the STEM-EDS maps. Interestingly, the Cu is colocalized with a small amount of Pd, in a 9:1 Cu:Pd ratio, although the Pd is predominantly present at the corners of the Pt nanocube seeds while the Cu appears more localized on the edges and corners of the cubes. At this point, Cu has deposited on the Pt seeds and Pd begins localizing at the corners, which are the most reactive regions of the Pt nanocubes where growth apparently is favored. Additionally, Cu is beginning to coalesce on the edges, which is also a highly reactive region of the seed particle surface. After 15 min at 170 ºC (Figure 2m-r), growth at the corners has increased to a point where an incomplete shell decorates the Pt

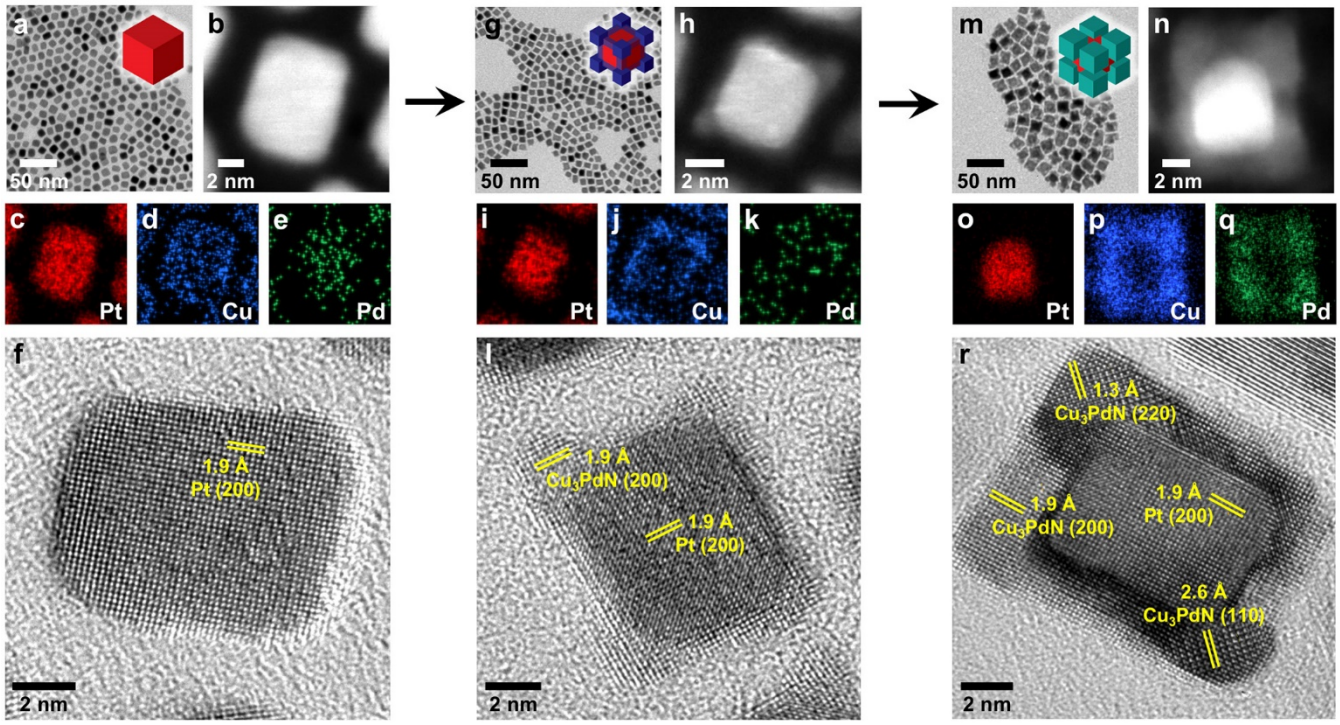

Figure 2. Time-dependent growth studies of Cu_3PdN on Pt nanocubes at 170 °C for (a-f) 5 minutes, (g-l) 10 minutes, and (m-r) 15 minutes. The data for each time point include (a,g,m) TEM images, (b,h,n) HAADF-STEM images, (c-e, i-k, o-q) STEM-EDS element maps for Pt (red), Cu (blue), and Pd (green), and (f,I,r) HRTEM images of individual particles. The STEM-EDS maps correspond to Pt-Lα, Cu-Kα, and Pd-Lα. HAADF-STEM and EDS maps were collected on a FEI Titan G2 S/TEM.

nanocube seeds. The corresponding STEM-EDS maps show co-localization of Cu and Pd in the 3:1 ratio expected for Cu_3PdN. XRD confirms the presence of both Pt and Cu_3PdN (Figure S5). Furthermore, the HRTEM image in Figure 2r shows lattice fringes on the corner domains with d-spacings corresponding to the (110) plane in Cu_3PdN. This d-spacing value, which is diagnostic of Cu_3PdN, matches well with the d-spacing of Cu_3PdN obtained from the Pt–Cu_3PdN XRD pattern, Figure S6. The HRTEM images show that Cu_3PdN and Pt are crystallographically aligned and epitaxial, which is consistent with the closely related lattice constants of Cu_3PdN (a = 3.85 Å) and Pt (a = 3.90 Å). While the presence of an amorphous Cu or CuO_x shell cannot be ruled out, the data are most consistent with the formation of Cu_3PdN.

The 60-minute and 120-minute samples, shown in Figure S4 of the Supporting Information, appear to be morphologically indistinguishable from the 15-minute sample, indicating that significant additional growth of Cu_3PdN on the Pt seeds does not occur, and that the terminal size is reached within 15 minutes of growth at 170 °C. However, XRD data shows an increase in relative peak intensity, implying increased crystallinity of the Cu_3PdN domains with increasing reaction time (Figure S5). This indicates that solution-phase annealing is occurring with prolonged heating.

XPS provides additional insights into the evolution of the surface species during the seeded growth process. Figures 3 and S7 show high-resolution XPS spectra of the Pt 4f, Cu 2p, Pd 3d, and N 1s regions for samples where Cu_3PdN growth on Pt was allowed to proceed at 170 °C for 10 minutes and 15 minutes. Quantification using instrumental relative sensitivity factors (RSFs) reveals 9:1 and 3:1 Cu:Pd ratios for the 10- and 15-minute samples, respectively, which matches the Cu:Pd ratios observed by EDS and is also consistent with the microscopic observation that Cu deposits before Pd.

For both the 10- and 15-minute samples, the XPS spectra of the N 1s region contain two distinct binding energies (Figure 3). The peak at ~397 eV corresponds to the N in Cu_3PdN and the peak at ~399.5 eV corresponds to the N in oleylamine that is adsorbed to the surfaces of the particles.[34] The N 1s signal for the 15-minute sample is more intense than for the 10-minute sample, with a significantly larger signal-to-noise ratio, and this is consistent with a larger amount of nitrogen incorporated into the product, consistent with the formation of Cu_3PdN, as the reaction proceeds. XPS spectra for the Pt 4f region (Figure S7 show the expected $4f_{5/2}$ and $4f_{7/2}$ binding energies of 74.5 eV and 71.2 eV, respectively, which are consistent with metallic Pt.[35] XPS spectra for the Cu 2p region shows the $2p_{1/2}$ and the $2p_{3/2}$ binding energies at 952.5 eV and 932.7 eV, respectively. The Cu 2p binding energies are in good agreement with those expected for Cu-N bonding in the Cu_3N substructure of Cu_3PdN.[32] The Pd 3d regions for both the 10- and 15-minutes samples show $3d_{3/2}$ and $3d_{5/2}$ binding energies of 340.7 eV and 335.4

eV, respectively. The peak at 335.4 eV corresponds well with the Pd-N binding energy that would be expected for the formation of Cu_3PdN, rather than a binding energy of 335.1 eV that would indicate metallic Pd.[34]

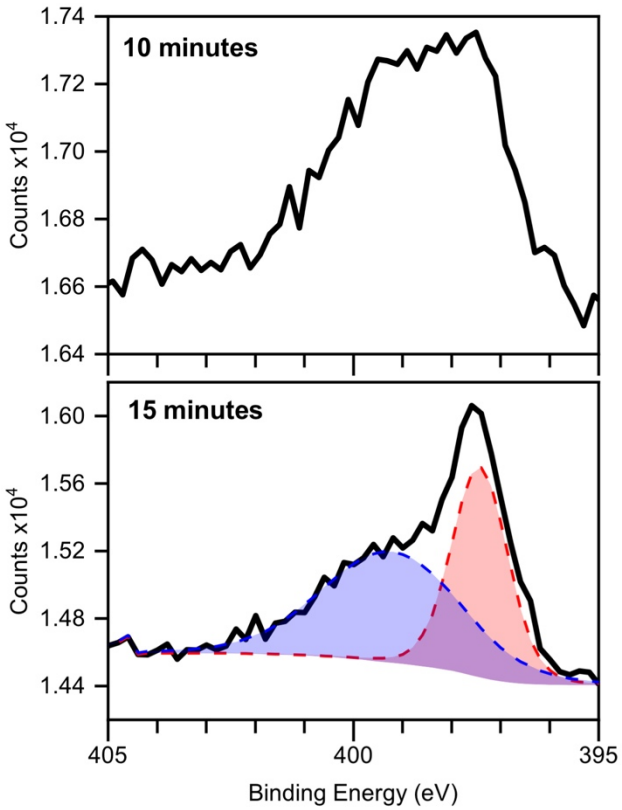

Figure 3. XPS spectra for the N 1s region characterizing the growth of Cu_3PdN on Pt nanocubes at 10- and 15-minute time points. The deconvolutions in the 15-minute sample represent the emission from surface bound oleylamine (blue) and N bonded to Cu in the Cu_3PdN crystal (red).

Taken together, the experiments and data described above provide important insights into the pathway by which Cu_3PdN grows on Pt nanoparticle seeds. Initially, a Cu-containing species deposits on the surface of the Pt seeds. As the reaction proceeds, more Cu is deposited, followed by a slower deposition and incorporation of Pd onto higher-energy regions of the Pt nanoparticle surface, i.e. corners of cubes or edges of multifaceted particles. Further heating results in coalescence of the Cu species with concomitant incorporation of deposited Pd, ultimately resulting in the formation and crystallization of Cu_3PdN. For the Pt cubes, this results in regioselective growth of Cu_3PdN on the corners. Continued heating beyond this point results in solution-phase annealing of the Cu_3PdN domains, which increases their crystallinity but does not result in further growth. The pathway by which Cu_3PdN grows on cube-shaped Pt seeds involves nonselective deposition followed by surface migration and coalescence to a preferred interface. A similar pathway was identified during the growth of Ag on Pt–Fe_3O_4 hybrid nanoparticles.[35] Here, Ag initially deposited on the both the Fe_3O_4 and Pt domains. Further heating resulted in surface migration of the Ag from the Fe_3O_4 domains to the Pt domains followed by coalescence into a larger Ag domain anchored to the Pt surface. It is also known that the morphology of a seed nanocrystal influences the morphology of the resulting heterostructure after seeded growth, due to differences in surface diffusion of deposited atoms as well as the nature of the particle-particle interface.[36,37]

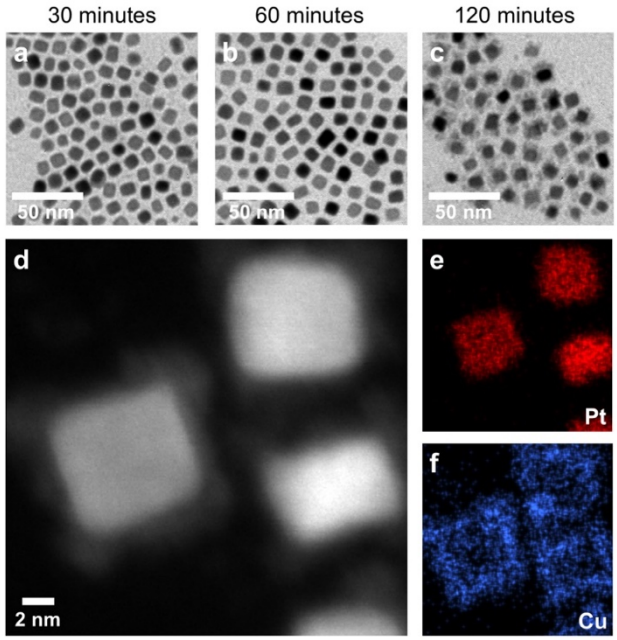

Figure 4. (a–c) TEM images characterizing the time-dependent growth of Cu_3N on Pt nanocubes at 170 ºC. (d) HAADF-STEM image and corresponding EDS maps for (e) Pt and (f) Cu) for the 120-minute sample. The STEM-EDS maps correspond to Pt-Lα and Cu-Kα.

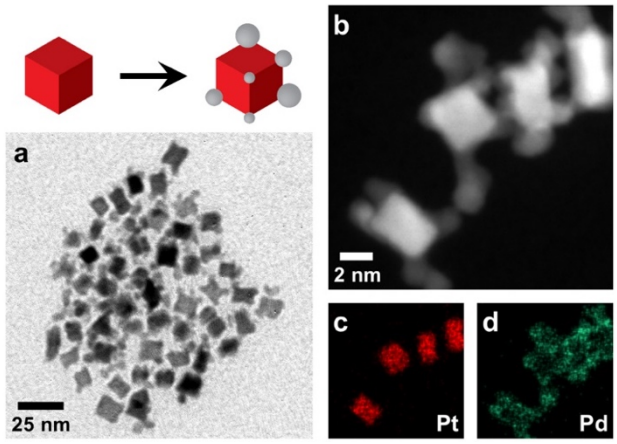

Figure 5. (a) TEM image, (b) HAADF-STEM image, and STEM-EDS maps for (c) Pt and (d) Pd corresponding to the growth of Pd on Pt nanocubes. The STEM-EDS maps correspond to Pt-Lα and Pd-Lα.

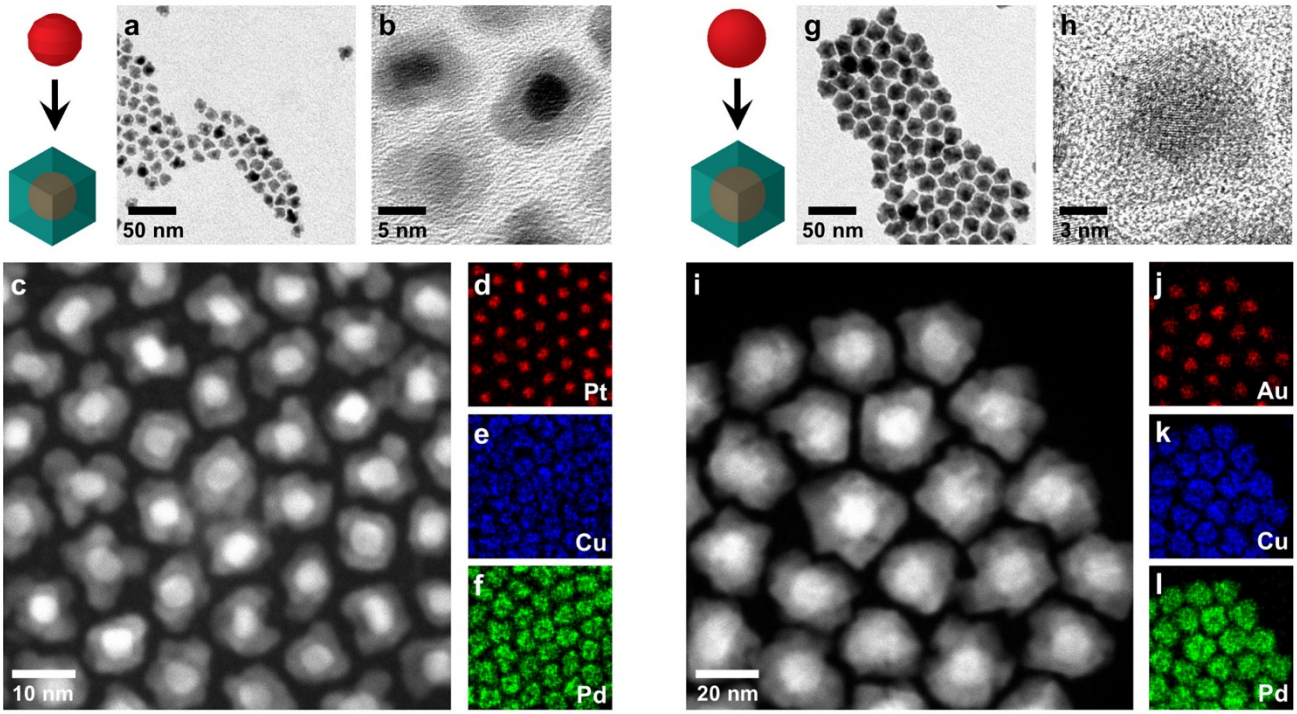

Figure 6. Growth studies of Cu_3PdN on (a–f) multifaceted Pt and (g–l) spherical Au. The data for each system include (a–b, g–h), TEM images, (c,i) HAADF-STEM images, and (d–f, j–l) STEM- EDS maps. The STEM-EDS maps correspond to Pt-Lα, Cu-Kα, and Pd-Lα.

Growth Pathway of Cu_3N and Pd on Pt Nanocubes. To better understand the role of Pd in facilitating the growth of Cu_3PdN on Pt, and also because Cu_3N and Cu_3PdN were observed to grow differently on Pt (Figure 1), we carried out analogous experiments growing Cu_3N and Pd. Figure 4 shows TEM images of the particles obtained during attempted growth of Cu_3N (without Pd) on Pt nanocubes for 30, 60, and 120 minutes at 170 ºC. No surface-seeded growth is observed at 30 and 60 minutes, but by 120 minutes there is evidence of growth. The HAADF-STEM image and STEM-EDS element maps in Figure 4 show that the Pt nanocubes are surrounded by a Cu-containing shell, and XRD and SAED data confirm the presence of both Pt and Cu_3N (Figure S8). The data in Figure 4 indicate that Cu_3N grows on both the corners and faces of the Pt nanocubes. This contrasts with the growth of Cu_3PdN, which was almost exclusively localized to the corners of the Pt nanocubes. However, a Cu-rich shell was observed to surround the Pt nanocubes at early time points during the growth of Cu_3PdN (Figure 2). This suggests that at early stages of the seeded-growth reactions, both Cu_3N and Cu_3PdN grow through a similar pathway, but that Pd plays a role in localizing further growth of Cu_3PdN to the corners of the Pt nanocubes, whereas for Cu_3N the growth remains indiscriminate.

TEM, HAADF-STEM, and STEM-EDS images for similar experiments involving the growth of Pd (without Cu_3N) on Pt are shown in Figure 5. The growth was carried out for 15 minutes at 170 ºC. The data reveal that Pd grows almost exclusively on the corners of the Pt nanocubes. This further validates the hypothesis that the seeded growth of Cu_3PdN on Pt nanocubes occurs first through Cu_3N growth on the entire Pt surface followed by selective deposition of Pd at the Pt nanocube corners and finally incorporation of the Cu_3N into the Pd to form Cu_3PdN.

Growth of Cu_3PdN on Multifaceted Pt and Spherical Au. The studies described above indicate that Cu_3PdN grows predominantly on the corners of Pt nanocubes, driven by the preference of Pd to deposit selectively at the corners during an intermediate step. This suggests that Cu_3PdN deposition on metal nanoparticle seeds that are more faceted or spherical, which do not have well-defined edges or corners, may not occur regioselectively, but rather form core-shell structures. To examine this behavior, 5 nm multifaceted Pt nanoparticles were subjected to the same Cu_3PdN growth conditions as outlined previously. Here, the only difference in the reaction is the initial morphology of the Pt seed particles. As shown in the TEM, HRTEM, HAADF-STEM, and STEM-EDS data in Figure 6, the dominant product is Pt@Cu_3PdN core@shell particles, with Cu_3PdN completely surrounding the multifaceted Pt nanoparticle seeds. However, a closer look reveals that the multifaceted Pt seeds span a range of morphologies, including nanocubes, multi-faceted particles, and spherical particles, allowing us to discern different growth patterns for different seed morphologies in the same sample and therefore under identical conditions. The nanocube-shaped seeds exhibit the same corner-

localized growth of Cu_3PdN that was observed in Figure 2, while the spherical seeds have a continuous shell of Cu_3PdN. Interestingly, the multi-faceted Pt seeds show preference for Cu_3PdN growth at the edges that connect different facets.

The results above confirm that faceting of seed nanoparticles influences subsequent growth and, consequently, that seed particle faceting can be used to tune the type of heterostructure that forms as a result of Cu_3PdN growth. Consistent with this, Figure 6 also shows data for Cu_3PdN growth on spherical Au nanoparticles, which do not exhibit significant faceting. Consistent with the role of faceting in growth location, Cu_3PdN completely surrounds the Au nanoparticles in an exclusive Au@Cu_3PdN core@shell morphology.

Growth of Cu_3PdN on Pt–Fe_3O_4 Heterodimers. The studies described above provide important insights into the pathway by which the ternary metal nitride Cu_3PdN can be controllably integrated into nanoparticle heterostructures. To further expand the complexity of such heterostructures, we applied our knowledge of Cu_3PdN seeded growth to Pt–Fe_3O_4, which is a more complex hybrid nanoparticle seed. Here, the same Pt nanocube seeds used as seeds for growing Cu_3PdN were first used to grow Fe_3O_4, as reported previously. Each resulting Pt–Fe_3O_4 heterodimer has a single domain of Fe_3O_4 that grows on a face of the Pt nanocube. The Fe_3O_4 domain protects one half of the Pt nanocube seed, leaving the other half exposed. We hypothesized, based on the studies above, that Cu_3PdN would grow on the corners of the exposed half of the Pt nanocube seed.

As shown in Figure 7, Cu_3PdN does indeed grow on the exposed surface of the Pt domain to form an unusual Fe_3O_4–Pt–Cu_3PdN heterotrimer. The TEM image in Figure 7a shows that the majority of the product is Fe_3O_4–Pt–Cu_3PdN, with small subpopulations of Pt–Fe_3O_4 and Pt–Cu_3PdN, which we anticipate could be separated through magnetic and/or thermal fractionation techniques if desired.[38] A representative HRTEM image, shown in Figure 7b, indicates that Cu_3PdN grows epitaxially on the corners and edges of the faceted Pt nanoparticle seeds, as expected based on the growth pathway and crystallographic relationships described in the preceding sections. Because on this pathway that favors growth at corners and edges, multiple distinct Cu_3PdN domains grow on the Pt seeds. The HAADF-STEM image in Figure 7c (inset) and corresponding STEM-EDS map in Figures 7d and Figure S9 further confirm the identities of the Fe_3O_4, Pt, and Cu_3PdN domains. The XRD data in Figure S9 confirm that all three components are present and crystalline throughout the bulk sample. Fe_3O_4 is the dominant phase by XRD, which is consistent with its crystallinity, size, and relative phase fraction in the Fe_3O_4–Pt–Cu_3PdN heterotrimers. The peaks for Pt and Cu_3PdN are close together but distinguishable, even within the significantly broadened peaks, based on the peak asymmetry.

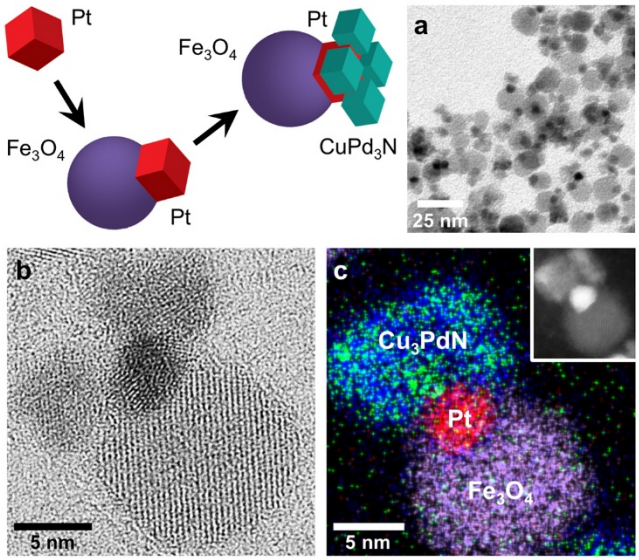

Figure 7. (a) TEM image, (b) HRTEM image, and (c) combined STEM-EDS map with corresponding HAADF-STEM (inset), characterizing the Cu_3PdN–Pt–Fe_3O_4 heterotrimer product formed from growing Cu_3PdN on Pt–Fe_3O_4 heterodimers. The STEM-EDS maps include Pt-Lα (red), Cu-Kα (blue), Pd-Lα (green), and Fe-Kα (purple). HAADF-STEM and EDS were collected on a FEI Titan G2 S/TEM.

Conclusions

We have shown that transition metal nitrides can be incorporated into colloidal nanoscale heterostructures through seeded growth on noble metal nanoparticles. We elucidated the pathways by which the model systems Cu_3N and Cu_3PdN grow on Pt and Au seeds and found that the types of nanostructures that form depend on both the morphology of the seed particle and the material being deposited. We found that Cu first deposits indiscriminately over the entire surface of the seed particles. For Cu_3PdN, Pd then deposits at corners or edges of faceted seed particles, followed by coalescence, growth, and crystallization that ultimately results in localization of Cu_3PdN to these higher-energy regions of the seed particle surface. When spherical Pt or Au seeds are used instead of cube-shaped or multifaceted particles, Cu_3PdN instead deposits on the entire surface rather than localized in certain regions. For Cu_3N on Pt, nonselective growth occurs as well, as Pd is not present to localize deposition to corners or facets. For Cu_3N on Au, Cu deposition competes with alloy formation, and we observe that AuCu forms instead of any heterogeneous growth product. Cu_3PdN can also be deposited on multicomponent seeds such as Fe_3O_4–Pt, forming complex Fe_3O_4–Pt–Cu_3PdN heterotrimers. Collectively, these insights provide guidelines for growing transition metal nitride nanoparticles on noble metal seeds, for tuning between core@shell and hybrid morphologies, and for using secondary metal deposition (e.g. Pd on Pt) to localize metal nitride growth at certain regions of the seed particle surface to achieve regioselective deposition. We anticipate that these pathways may be generalizable to other metal–

metal nitride systems, and also be useful for developing multi-functional nanostructures that exploit the catalytic and plasmonic properties of the various components.

ASSOCIATED CONTENT

Supporting Information. Additional TEM, XRD, and XPS data. This material is available free of charge via the Internet at http://pubs.acs.org.

AUTHOR INFORMATION

Corresponding Author

* R. E. Schaak. Email: res20@psu.edu

Notes

The authors declare no competing financial interest.

ACKNOWLEDGMENT

This work was supported by the U.S. National Science Foundation under Grant CHE-1707830. TEM imaging was performed in the Penn State Microscopy and Cytometry facility. HR-TEM imaging, S/TEM imaging, and EDS mapping were performed at the Materials Characterization Lab of the Penn State Materials Research Institute. The authors thank Dr. Jamie Chen for helpful discussions.

REFERENCES

(1) Zhou, M.; Wang, H.; Elnabawy, A. O.; Hood, Z. D.; Chi, M.; Xiao, P.; Zhang, Y.; Mavrikakis, M.; Xia, Y. Facile One-Pot Synthesis of Pd@Pt_{1L} Octahedra with Enhanced Activity and Durability toward Oxygen Reduction. *Chem. Mater.* **2019**, *31*, 1370–1380 DOI: 10.1021/acs.chemmater.8b04756.

(2) Xia, X.; Xie, S.; Liu, M.; Peng, H.-C.; Lu, N.; Wang, J.; Kim, M. J.; Xia, Y. On the Role of Surface Diffusion in Determining the Shape or Morphology of Noble-Metal Nanocrystals. *Proc. Natl. Acad. Sci.* **2013**, *110*, 6669-6673 DOI: 10.1073/pnas.1222109110.

(3) Yang, X.; Roling, L. T.; Vara, M.; Elnabawy, A. O.; Zhao, M.; Hood, Z. D.; Bao, S.; Mavrikakis, M.; Xia, Y. Synthesis and Characterization of Pt–Ag Alloy Nanocages with Enhanced Activity and Durability toward Oxygen Reduction. *Nano Lett.* **2016**, *16*, 6644–6649 DOI: 10.1021/acs.nanolett.6b03395.

(4) Buck, M. R.; Schaak, R. E. Emerging Strategies for the Total Synthesis of Inorganic Nanostructures. *Angew. Chem. Int. Ed.* **2013**, *52*, 6154–6178 DOI: 10.1002/anie.201207240.

(5) Banin, U.; Ben-Shahar, Y.; Vinokurov, K. Hybrid Semiconductor–Metal Nanoparticles: From Architecture to Function. *Chem. Mater.* **2014**, *26*, 97–110 DOI: 10.1021/cm402131n.

(6) Amirav, L.; Alivisatos, A. P. Photocatalytic Hydrogen Production with Tunable Nanorod Heterostructures. *J. Phys. Chem. Lett.* **2010**, *1*, 1051–1054 DOI: 10.1021/jz100075c.

(7) Cathcart, N.; Murshid, N.; Campbell, P.; Kitaev, V. Selective Plasmonic Sensing and Highly Ordered Metallodielectrics via Encapsulation of Plasmonic Metal Nanoparticles with Metal Oxides. *ACS Appl. Nano Mater.* **2018**, *1*, 6514–6524 DOI: 10.1021/acsanm.8b01964.

(8) Deka, K.; Guleria, A.; Kumar, D.; Biswas, J.; Lodha, S.; Kaushik, S. D.; Choudhary, S. A.; Dasgupta, S.; Deb, P. Janus Nanoparticles for Contrast Enhancement of T_1–T_2 Dual Mode Magnetic Resonance Imaging. *Dalton Trans.* **2019**, *48*, 1075–1083 DOI: 10.1039/C8DT04038A.

(9) Fernando, J. F. S.; Shortell, M. P.; Firestein, K. L.; Zhang, C.; Larionov, K. V.; Popov, Z. I.; Sorokin, P. B.; Bourgeois, L.; Waclawik, E. R.; Golberg, D. V. Photocatalysis with Pt–Au–ZnO and Au–ZnO Hybrids: Effect of Charge Accumulation and Discharge Properties of Metal Nanoparticles. *Langmuir* **2018**, *34*, 7334–7345 DOI: 10.1021/acs.langmuir.8b00401.

(10) Pang, F.; Zhang, R.; Lan, D.; Ge, J. Synthesis of Magnetite–Semiconductor–Metal Trimer Nanoparticles through Functional Modular Assembly: A Magnetically Separable Photocatalyst with Photothermic Enhancement for Water Reduction. *ACS Appl. Mater. Inter.* **2018**, *10*, 4929–4936 DOI: 10.1021/acsami.7b17046.

(11) Oh, N.; Kim, B. H.; Cho, S.-Y.; Nam, S.; Rogers, S. P.; Jiang, Y.; Flanagan, J. C.; Zhai, Y.; Kim, J.-H.; Lee, J.; et al. Double-Heterojunction Nanorod Light-Responsive LEDs for Display Applications. *Science* **2017**, *355*, 616-619 DOI: 10.1126/science.aal2038.

(12) Gordon, T. R.; Schaak, R. E. Synthesis of Hybrid Au-In_2O_3 Nanoparticles Exhibiting Dual Plasmonic Resonance. *Chem. Mater.* **2014**, *26*, 5900–5904 DOI: 10.1021/cm502396d.

(13) Maiti, K.; Balamurugan, J.; Peera, S. G.; Kim, N. H.; Lee, J. H. Highly Active and Durable Core–Shell Fct-PdFe@Pd Nanoparticles Encapsulated NG as an Efficient Catalyst for Oxygen Reduction Reaction. *ACS Appl. Mater. Inter.* **2018**, *10*, 18734–18745 DOI: 10.1021/acsami.8b04060.

(14) Gilroy, K. D.; Ruditskiy, A.; Peng, H.-C.; Qin, D.; Xia, Y. Bimetallic Nanocrystals: Syntheses, Properties, and Applications. *Chem. Rev.* **2016**, *116*, 10414–10472 DOI: 10.1021/acs.chemrev.6b00211.

(15) Habas, S. E.; Lee, H.; Radmilovic, V.; Somorjai, G. A.; Yang, P. Shaping Binary Metal Nanocrystals through Epitaxial Seeded Growth. *Nat. Mater.* **2007**, *6*, 692–697 DOI: 10.1038/nmat.1957.

(16) Motl, N. E.; Bondi, J. F.; Schaak, R. E. Synthesis of Colloidal Au–Cu_2S Heterodimers via Chemically Triggered Phase Segregation of AuCu Nanoparticles. *Chem. Mater.* **2012**, *24*, 1552–1554 DOI: 10.1021/cm300511q.

(17) Fenton, J. L.; Steimle, B. C.; Schaak, R. E. Tunable Intraparticle Frameworks for Creating Complex Heterostructured Nanoparticle Libraries. *Science* **2018**, *360*, 513-517 DOI: 10.1126/science.aar5597.

(18) Fenton, J. L.; Hodges, J. M.; Schaak, R. E. Synthetic Deconvolution of Interfaces and Materials Components in Hybrid Nanoparticles. *Chem. Mater.* **2017**, *29*, 6168–6177. DOI: 10.1021/acs.chemmater.7b02556.

(19) Buck, M. R.; Bondi, J. F.; Schaak, R. E. A Total-Synthesis Framework for the Construction of High-Order Colloidal Hybrid Nanoparticles. *Nat. Chem.* **2012**, *4*, 37-44 DOI: 10.1038/nchem.1195

(20) Roman, B. J.; Otto, J.; Galik, C.; Downing, R.; Sheldon, M. Au Exchange or Au Deposition: Dual Reaction Pathways in Au–$CsPbBr_3$ Heterostructure Nanoparticles. *Nano Lett.* **2017**, *17*, 5561–5566 DOI: 10.1021/acs.nanolett.7b02355.

(21) Hernández-Pagán, E. A.; Leach, A. D. P.; Rhodes, J. M.; Sarkar, S.; Macdonald, J. E. A Synthetic Exploration of Metal–Semiconductor Hybrid Particles of $CuInS_2$. *Chem. Mater.* **2015**, *27*, 7969–7976 DOI: 10.1021/acs.chemmater.5b03142.

(22) Wu, H.; Chen, W. Copper Nitride Nanocubes: Size-Controlled Synthesis and Application as Cathode Catalyst in Alkaline Fuel Cells. *J. Am. Chem. Soc.* **2011**, *133*, 15236–15239 DOI: 10.1021/ja204748u.

(23) Abeysinghe, D.; Skrabalak, S. E. Toward Shape-Controlled Metal Oxynitride and Nitride Particles for Solar Energy Applications. *ACS Energy Lett.* **2018**, *3*, 1331–1344 DOI: 10.1021/acsenergylett.8b00518.

(24) Balogun, M.-S.; Qiu, W.; Wang, W.; Fang, P.; Lu, X.; Tong, Y. Recent Advances in Metal Nitrides as High-Performance Electrode Materials for Energy Storage Devices. *J. Mater. Chem. A* **2015**, *3*, 1364–1387 DOI: 10.1039/C4TA05565A.

(25) Chaudhuri, K.; Shaltout, A.; Shah, D.; Guler, U.; Dutta, A.; Shalaev, V. M.; Boltasseva, A. Photonic Spin Hall Effect in Robust Phase Gradient Metasurfaces Utilizing Transition Metal Nitrides. *ACS Photonics* **2019**, *6*, 99–106 DOI: 10.1021/acsphotonics.8b00943.

(26) Chen, Y.; Landes, N. T.; Little, D. J.; Beaulac, R. Conversion Mechanism of Soluble Alkylamide Precursors for the Synthesis of Colloidal Nitride Nanomaterials. *J. Am. Chem. Soc.* **2018**, *140*, 10421–10424 DOI: 10.1021/jacs.8b06063.

(27) Egeberg, A.; Warmuth, L.; Riegsinger, S.; Gerthsen, D.; Feldmann, C. Pyridine-Based Low-Temperature Synthesis of CoN, Ni_3N and Cu_3N Nanoparticles. *Chem. Commun.* **2018**, *54*, 9957–9960 DOI: 10.1039/C8CC04893B.

(28) Vaughn II, D. D.; Araujo, J.; Meduri, P.; Callejas, J. F.; Hickner, M. A.; Schaak, R. E. Solution Synthesis of Cu_3PdN Nanocrystals as Ternary Metal Nitride Electrocatalysts for the Oxygen Reduction Reaction. *Chem. Mater.* **2014**, *26*, 6226–6232 DOI: 10.1021/cm5029723.

(29) Sithole, R. K.; Machogo, L. F. E.; Airo, M. A.; Gqoba, S. S.; Moloto, M. J.; Shumula, P.; Van Wyk, J.; Moloto, N. Synthesis and Characterization of Cu_3N Nanoparticles Using pyrrole-2-carbaldpropyliminato Cu(II) complex and $Cu(NO_3)_2$ as Single-Source Precursors: the Search for an Ideal Precursor. *New J. Chem.*, **2018**, *42*, 3042-3049. DOI: 10.1039/C7NJ05181F.

(30) Deshmukh, R.; Zeng, G.; Tervoort, E.; Staniuk, M.; Wood, D.; Niederberger, M. Ultrasmall Cu_3N Nanoparticles: Surfactant-Free Solution-Phase Synthesis, Nitridation Mechanism, and Application for Lithium Storage. *Chem. Mater.,* **2015**, *27*, 8282-8288. DOI: 10.1021/acs.chemmater.5b03444.

(31) Wang, C.; Daimon, H.; Onodera, T.; Koda, T.; Sun, S. A General Approach to the Size- and Shape-Controlled Synthesis of Platinum Nanoparticles and Their Catalytic Reduction of Oxygen. *Angew. Chem. Int. Ed.* **2008**, *47*, 3588–3591 DOI: 10.1002/anie.200800073.

(32) Peng, S.; Lee, Y.; Wang, C.; Yin, H.; Dai, S.; Sun, S. A Facile Synthesis of Monodisperse Au Nanoparticles and Their Catalysis of CO Oxidation. *Nano Res.* **2008**, *1*, 229–234 DOI: 10.1007/s12274-008-8026-3.

(33) Hodges, J. M.; Morse, J. R.; Fenton, J. L.; Ackerman, J. D.; Alameda, L. T.; Schaak, R. E. Insights into the Seeded-Growth Synthesis of Colloidal Hybrid Nanoparticles. *Chem. Mater.* **2017**, *29*, 106–119 DOI: 10.1021/acs.chemmater.6b02795.

(34) Ji, A. L.; Lu, N. P.; Gao, L.; Zhang, W. B.; Liao, L. G.; Cao, Z. X. Electrical Properties and Thermal Stability of Pd-Doped Copper Nitride Films. *J. Appl. Phys.* **2013**, *113*, 043705 DOI: 10.1063/1.4788905.

(35) Schick, I.; Lorenz, S.; Gehrig, D.; Schilmann, A.-M.; Bauer, H.; Panthöfer, M.; Fischer, K.; Strand, D.; Laquai, F.; Tremel, W. Multifunctional Two-Photon Active Silica-Coated Au@MnO Janus Particles for Selective Dual Functionalization and Imaging. *J. Am. Chem. Soc.* **2014**, *136*, 2473–2483 DOI: 10.1021/ja410787u.

(36) Weiner, R. G.; Kunz, M. R.; Skrabalak, S. E. Seeding a New Kind of Garden: Synthesis of Architecturally Defined Multimetallic Nanostructures by Seed-Mediated Co-Reduction. Acc. Chem. Res., 2015, 48, 2688-2695. DOI: 10.1021/acs.accounts.5b00300.

(37) Chen, A. N.; Scanlan, M. M.; Skrabalak, S. E. Surface Passivation and Supersaturation: Strategies for Regioselective Deposition in Seeded Synthesis. *ACS Nano*, **2017**, *11*, 12624-12631. DOI: 10.1021/acsnano.7b07041.

(38) Smith, W. C.; Morse, J. R.; Bria, C. R. M.; Schaak, R. E.; Williams, S. K. R. Composition-Based Separation of Pt–Fe_3O_4 Hybrid Nanoparticles by Thermal Field-Flow Fractionation. *ACS Appl. Nano Mater.* **2018**, *1*, 6435–6443. DOI: 10.1021/acsanm.8b01643.

Table of Contents (TOC) Graphic